ADVANCED MATERIALS
www.advmat.de

Direct Observation of Optically Active Mid-Gap Electronic States in Hexagonal Boron Nitride by Electron Spectroscopy

Sakal Singla, Pragya Joshi, Gabriel I. López-Morales, Kenji Watanabe, Takashi Taniguchi, Cyrus E. Dreyer, and Biswanath Chakraborty**

Optically active point defects in wide-bandgap semiconductors have been demonstrated to be attractive for a variety of quantum and nanoscale applications. In particular, color centers in hexagonal boron nitride (hBN) have recently gained substantial attention owing to their spectral tunability, brightness, stability, and room-temperature operation. Despite all of the recent studies, precise detection of the defect-induced mid-gap electronic states (MESs) and their simultaneous correlations with the observed emission in hBN remain elusive. Directly probing these MESs provides a powerful approach toward atomic identification and optical control of the defect centers underlying the sub-bandgap emission in hBN. Combining optical and electron spectroscopy, the existence of mid-gap absorptive features is revealed at the emissive sites in hBN, along with an atom-by-atom identification of the underlying defect configuration. The atomically resolved defect structure, primarily constituted by vacancies and carbon/oxygen substitutions, is further studied via first-principles calculations, which support the correlation with the observed MESs through the electronic density of states. This work provides a direct relationship between the observed visible emission in hBN, the underlying defect structure, and its absorptive MESs, opening venues for atomic-scale and optical control in hBN for quantum technology.

1. Introduction

Defects modulate the optical and electrical properties of insulators, including the optical absorption/emission, dielectric response, electrical conductivity, mobility, and carrier concentration. Especially in wide-bandgap materials, defects often create mid-gap electronic states (MESs), which introduce irreversible loss of carriers through charge trapping, non-radiative recombination, and sub-bandgap radiative transitions. Also, MESs can be addressed to generate quantum emission; some examples include the nitrogen-vacancy center in diamond,[1–3] gallium or nitrogen vacancies in gallium nitride (GaN),[4,5] vacancies in silicon carbide (SiC),[6–9] defects in zinc oxide (ZnO),[10] and vacancies or impurities in hexagonal boron nitride (hBN).[11,12]

The nature and energies of the MESs depend on their microscopic structure and chemical composition. Therefore, the direct probes of the defects and their MESs are necessary to optimize the optical and electronic properties of materials. Due to their burgeoning applications in quantum technologies, precision spectroscopy of defects has experienced renewed interest. In particular, hBN has been proposed as a promising material for developing room-temperature quantum devices because of its high thermal and air stability, combined with ease of integration with photonic structures on a chip.[13,14] Midgap states in hBN have emerged as multifunctional candidates, serving as single photon emitters while also showing great promise in nanoscale magnetometry, enabling the development of next-generation photonic quantum technologies.[15–21] A comprehensive understanding of MESs in hBN is also important to the field of material design for designing defect-tolerant dielectrics and engineered insulators.[22]

A range of processing techniques[23–28] are utilized for creating point defects and corresponding MESs in hBN, which are capable of emission over a wide sub-bandgap spectral range (300–800 nm).[29,30] Using photoluminescence (PL)[11,28,31] and cathodoluminescence (CL),[32,33] these spectroscopic features have been explored extensively. However, any direct visualization of the optically active MESs and their correspondence to the underlying defect configuration remains challenging due to experimental limitations. Although various experimental techniques

S. Singla, P. Joshi, B. Chakraborty
Department of Physics
Indian Institute of Technology Jammu
Jammu, Jammu and Kashmir 181221, India
E-mail: biswanath.chakraborty@iitjammu.ac.in

G. I. López-Morales, C. E. Dreyer
Department of Physics and Astronomy
Stony Brook University
Stony Brook, NY 11794, USA
E-mail: cyrus.dreyer@stonybrook.edu

K. Watanabe
Research Center for Functional Materials
National Institute for Materials Science
1-1 Namiki, Tsukuba 305-0044, Japan

T. Taniguchi
International Center for Materials Nanoarchitectonics
National Institute for Materials Science
1-1 Namiki, Tsukuba 305-0044, Japan

C. E. Dreyer
Center for Computational Quantum Physics
Flatiron Institute
162 5th Avenue, New York, NY 10010, USA

The ORCID identification number(s) for the author(s) of this article can be found under https://doi.org/10.1002/adma.202502342

DOI: 10.1002/adma.202502342

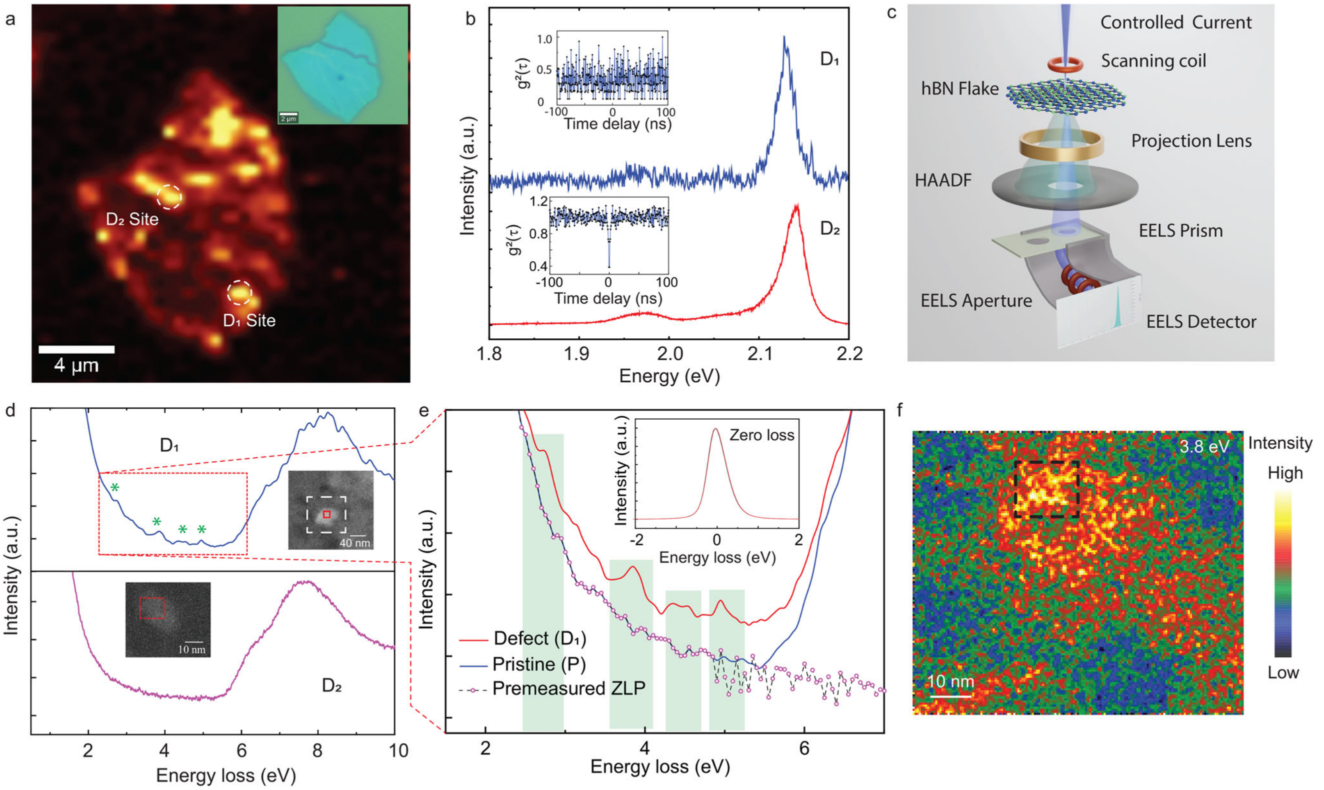

Figure 1. Spectroscopic analysis of the emissive regions in the hBN flake. a) Scanning PL map of the hBN flake. The inset provides an optical image of the same sample region. b) Spectrum for the defect sites D_1 and D_2. c) Cartoon of experimental geometry used to observe mid-gap electronic states. d) Valance EELS spectra for D_1 and D_2 (top and bottom, respectively). Inset: HAADF-STEM micrograph from where the spectrum is collected. e) Valance EELS spectra for D_1 site compared to that of pristine hBN. The inset shows the zero-loss peak (ZLP) for both spectra. Zoomed marked region which directly reveals the formation of mid-gap electronic states. f) Low-loss energy mapping for D_1 site centered around 3.8 eV. The black dashed box delineates the region from which the core-loss analysis is carried out.

(e.g., angle-resolved photoemission spectroscopy (ARPES),[34–37] hard X-ray photoelectron spectroscopy (HAXPES), deep-level transient spectroscopy,[38] resonant tunnel spectroscopy[39]) probe the MESs, they fail to reveal the relevant microscopic structure. Scanning tunneling microscope (STM) overcomes this difficulty by resolving both the electronic states and the defect structure,[40,41] it lacks in the exact elemental identification of the impurities present.

Alternatively, aberration-corrected scanning transmission electron microscopy (STEM) coupled with electron energy loss spectroscopy (EELS) offers new opportunities for probing at the nanoscale the defect energy levels,[42–44] local atomic structure, and chemical species;[44–49] these can be coupled to the optical activity via correlation with specific emissive location.[50] In this case, the electron beam interaction with the sample triggers various inelastic scattering processes. Based on the energy of the in-elastically scattered electron signal, the underlying process can be categorized, e.g., low-loss region (phonon vibrations, intra-bandgap transition, plasmon excitation) and core-loss region (elemental composition). Thus, for optically active defects in hBN, STEM-EELS can be utilized directly to probe the MESs, as well as local structures with their chemical species, with atomic resolution.

In this work, we combine high-resolution EELS and PL spectroscopy to directly probe defects responsible for the visible emission in hBN. With the application of low-loss EELS, we capture the energy loss from defects in hBN and further analyze it via Kramers–Kronig relations. We also perform high-angle annular dark field (HAADF) imaging and spatially-resolved core-loss EELS spectroscopy to determine the defect structure of the emission location. Lastly, first-principles calculations based on the experimentally imaged defect structure support a connection between its individual defect constituents and the observed MESs.

2. Results and Discussion

Following earlier reports, to create optically-active defect centers, an exfoliated hBN flake (~ 25 nm thick from atomic force microscope (AFM) analysis) is subjected to electron-beam irradiation in a field-emission scanning electron microscope and annealed subsequently at 850° C under an argon atmosphere.[50,51] Further details regarding sample fabrication are given in the Experimental Section. The flake was scanned for any observable emission which would also confirm the presence of point-defect sites. A confocal PL scan of the flake is shown in **Figure 1a**. The PL spectra in Figure 1b acquired from two locations namely D_1 and D_2 exhibits different spectral characteristics. Notably, the stronger emission from D_2 resembles quantum character with photon anti-bunching; the second-order auto-correlation from emission collected at this site (Figure 1b, inset) shows 0.4 at zero-time delay ($g^2(0)$) confirming single photon emission (SPE) from site D_2. Such quantum behavior is absent in the emission collected from D_1. The emissions from both sites are in the visible range, while hBN has an electronic bandgap of around 6 eV. It can thus be concluded that the observed emission is due to radiative transitions involving energy states that lie within the bandgap of hBN and are known to be created by defect sites. The difference in the spectral profiles from each site can be attributed to differences in their local defect environments (defect concentration, atomic arrangements, etc.).

In an attempt to probe the defect-induced MESs, we carried out low-loss EELS measurements on the hBN flake. The setup is illustrated in Figure 1c. The low-loss region of the EELS spectra, which typically stretches from 0 to 50 eV, gives information about the dielectric properties of the specimen, including the bandgap, phonon and plasmon energies. The low-loss region is characterized by a strong zero-loss peak (ZLP) originating from elastic scattering of the incident electrons, which could exhibit a broad energy spread reaching up to 2 eV. In order to capture any distinct energy-loss features, it is desirable to achieve a narrow linewidth of the ZLP to prevent any overlapping. Our TEM is equipped with a cold field emission gun (c-FEG), which allows to achieve low energy spread of the electron beam. Further reduction in ZLP linewidth was done by: (i) reducing the operational voltage up to 80 kV; (ii) decreasing the emission current of the probe (15 μA → 4.6 μA); (iii) shifting the bright disk from the high-resolution EELS entrance aperture (diameter ~ 2.5 mm).[52–54] Overall, we could achieve a ZLP full-width half maximum (FWHM) of ~ 0.5 eV by operating the TEM with the above-mentioned parameters, enabling us to resolve features with energies from 1 eV onward and capture the MES in hBN flake. Operating under these conditions also allows the suppression of Cerenkov radiation from the sample[55] and minimizes possible effects from sample damage. Additional details regarding the FWHM reduction are included in the Experimental Section.

The flake was transferred to a holey carbon-coated TEM grid, and the emission regions D_1 and D_2 were located (details discussed in the Supporting Information, Section S1). Low-loss EELS spectra in Figure 1d from the site D_1 and D_2 show the distinct band-edge around 5.5 eV. Interestingly, for the D_1 region, distinct features (representing energy loss) appeared within the bandgap centered around 2.8, 3.8, 4.2, and 5 eV (marked by the dotted rectangular box). To ascertain that the observed mid-gap features are not associated with noise or artifact, we compared spectra from D_1 to that from a pristine region (free from defects) and the pre-measured ZLP (direct beam without sample). As shown in Figure 1e, the pristine and pre-measured spectra are almost merged (for regions within the hBN bandgap), while the MES spectral features in the D_1 spectrum are well resolved from the background. We could not observe any sub-bandgap features in the low-loss EELS from D_2, perhaps limited by the detector resolution. Figure 1f shows the spatial profile (low loss energy map) of the midgap state centered around 3.8 eV and helps identifying the defect complex across site D_1. The squared marked region which is characterized by strong presence of the energy feature is analyzed further. The remaining energy loss maps corresponding to 2.8, 4.2, and 5 eV are included in the Supporting Information (Section S6).

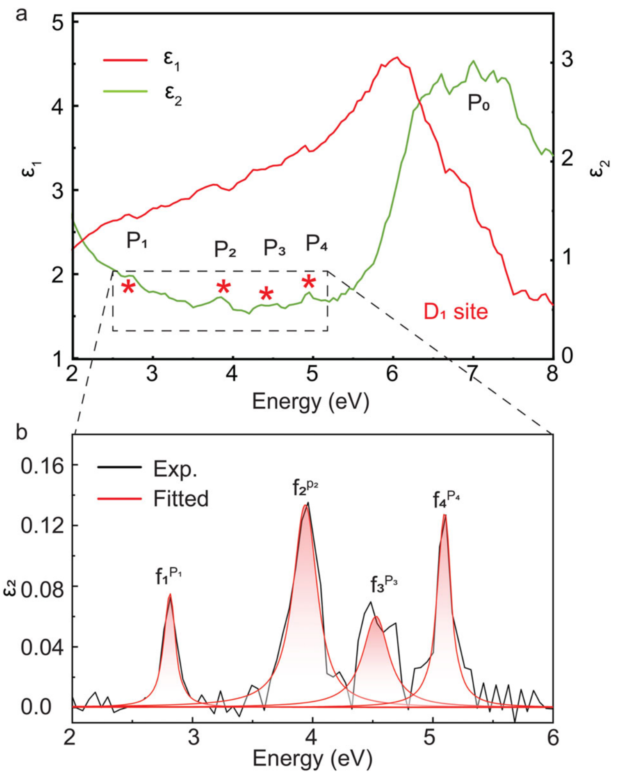

Figure 2. a) Real (red line) and imaginary (green line) components of the dielectric function for the D_1 site, as calculated from Kramers–Kronig relations. b) Baseline corrected ϵ_2 (black line) along with the fit from a Lorentzian oscillator model (red line).

To analyze the absorptive MESs, we estimate the dielectric function from the low-loss spectrum using the Kramers–Kronig relationship.[56] **Figure 2a** shows the real (ϵ_1) and complex (ϵ_2) parts of the dielectric function, as extracted from the low-loss EELS spectrum collected from site D_1. Resolvable peaks in ϵ_2 indicate mid-gap absorption (MESs). To quantify the absorption, the imaginary dielectric part is fitted via a Lorentz oscillator model,[57] where the oscillator strength corresponding to each absorption (f_i) is used as a fitting parameter. Figure 2b shows the fitted ϵ_2 extracted from the region of interest, highlighted by the rectangular box in Figure 2a. For reference, the oscillator strength ratios (with respect to the hBN band-edge transition) are included in the Supporting Information (Section S2). The same analysis is performed on the pristine hBN low-loss signal. In this case, MES-mediated energy loss below the bandgap edge is absent. Further details are included in Section S2.1 (Supporting Information).

We now turn to the chemical and physical nature of the defects responsible for the MESs. We begin with a low-resolution EELS mapping of the D_1 site to uncover the presence of foreign species in the hBN lattice. **Figure 3a** shows scattered presence of carbon along with traces of oxygen localized over a small region (white dashed circle). Subsequently, we focus on this encircled region and captured a core-loss EELS spectrum and spatial elemental mapping (see Figure 3b). Such a spectrum in Figure 3c also confirmed the presence of carbon and oxygen: a prominent carbon K-edge signal around 285 eV and a faint oxygen K-edge signal around 532 eV. Not only the presence of impurities, but also how

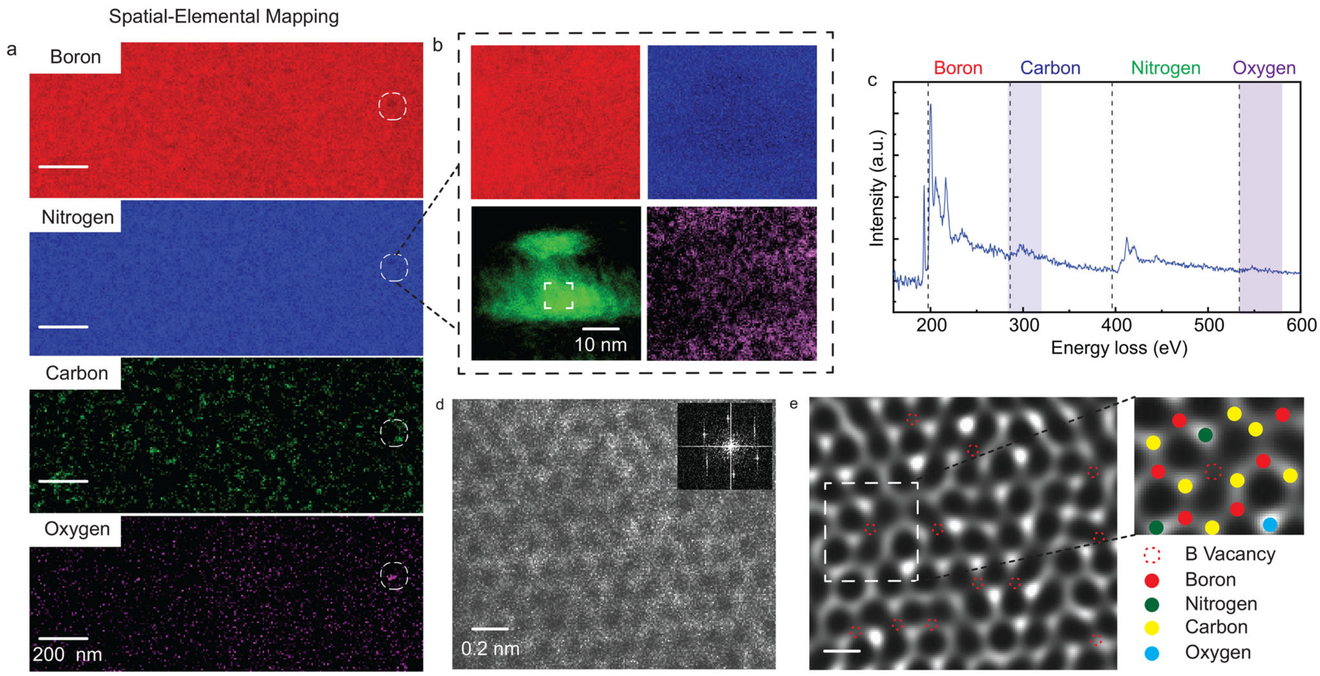

Figure 3. a) Spatial elemental mapping around the D_1 site. The HAADF STEM micrograph for this region is given in the Supporting Information, Section S4.1. The mapping area is marked by the red dotted square box. b,c). Zoomed spatial elemental mapping and EELS spectra of the dotted circle marked in Figure 3a respectively. d) High-resolution STEM micrograph from the white colored marked frame in Figure 3b. inset: fast Fourier transformation of same region. e. Inverse fast Fourier transformed image. Inset right panel: final identification of elemental species, based on the core-loss signal and HAADF intensities.

they are arranged in the hBN lattice plays a vital role in understanding the emergence of the MESs. To address the local atomic level picture, we did high-resolution atomic number (Z) contrast HAADF-STEM imaging of the same region. Figure 3d shows the HAADF-STEM micrograph where hexagons are visible. Enhancing signal-to-noise ratio by fast Fourier transformation (FFT) and its inverse, we obtained a significantly better resolution resolving each atomic site. Several vacancies (red dash circles) and isolated bright lattice sites are observed in Figure 3e. Note that the atomic incoherent elastic scattering is directly proportional to Z.

Based on this, each atom presents a different contrast (intensity), i.e., lighter atoms appear darker than the heavier ones. While the core-loss spectrum confirmed the impurities, Z contrast imaging tells us about their apparent locations in the hBN lattice. Oxygen, being the heaviest of the atomic species observed, looks significantly brighter than rest of the atoms, while boron yields the least contrast. Using the intensity of their inherent elastic and inelastic scattering, we identify the position of each atomic species across the defect site. For reference, The utilized HAADF line intensity profiles and core loss signal for identifying atomic species are provided in the Supporting Information, Section S5. The final intensity-based identification of the region underlying the observed MESs (white dotted square in Figure 3e) is shown in the inset of Figure 3e, highlighting a cluster of defects with significant contents of oxygen and carbon. We also find numerous boron vacancies within this region. A complete picture of the identified atomic species at the defect site is provided in the Supporting Information, Section S5.

The correlation between PL and TEM on D_1 and D_2 sites is governed by their relative defect density. The comparison of relative defect density is tabulated in the Supporting Information, Section S4.2. In D_1 site, we clearly see from the HAADF-STEM and EELS maps that there is a high density of defects and impurities. This results in a significant density of states for absorption, resulting in the observed peaks in the low-loss valence EELS spectra. D_2 site on the other hand, must have a much lower defect density, since no such peaks are observed. The fact that the defects are more dilute explains the observed SPE in the D_2 PL, and the much larger luminescence intensity (due to reduction in non-radiative pathways compared to D_1 site).

2.1. First-Principles Calculations

We employ ab initio calculations based on density functional theory (DFT) to further validate the experimental defect configuration proposed to be responsible for the observed MESs (Figure 3e). All specific computational details are included in the Experimental Section. Of course, the full defect structure presented in Figure 3e is prohibitively large for an explicit DFT calculation. Thus, an approximation must be made to break this system into manageable calculations. We make the assumption that the large hetero-specie cluster observed in Figure 3e can be described via individual atomic-size point defects and approximate defect-defect interactions between these. In particular, we combine calculations of isolated point defects and isolated nearest-neighbor complexes to get an approximate picture of the

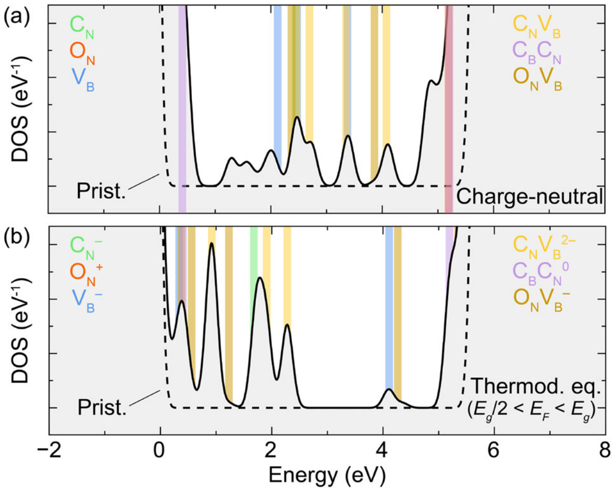

Figure 4. Average electronic density of states (DOS) as calculated from density functional theory (DFT). a) Charge-neutral configuration of defects, based on the atomic identification in Figure 3e. b) The charged version of (a) in thermodynamic equilibrium, based on previously calculated formation energies and a Fermi level close to the conduction band (typical hBN sample). The vertical shades are color-coded with the individual defects they correspond to. The DOS of pristine hBN is overlaid (dashed black lines) as a reference.

properties of the cluster. Further, we estimate some of the defect–defect interactions within the cluster by performing explicit DFT calculations for select defect pairs at different inter-defect distances (see Supporting Information, Section S8). These approximations can be justified by the tightly localized (and mostly out-of-plane) atomic-like orbitals that describe the electrons in most hBN point defects studies thus far,[58–61] which include most of those found to comprise the full defect complex proposed in our experiments. We note that recent DFT calculations with similar computational parameters show that when considering defect clusters in hBN explicitly, most of the defects' electronic structure remain similar to their isolated forms.[50,60,62–65]

Based on our assumptions, the absorptive MES features observed arise as a linear combination of the states of the individual defects; we take the weights to correspond roughly to the observed relative density of defects/complexes, and consider just the DFT density of states (DOS) for simplicity. We add approximate defect-defect interactions by randomized sampling of defect-pairs while accumulating the average DOS of the full cluster (further details in Supporting Information, Section S8). The results are presented in **Figure 4**. Here, shaded regions represent energy windows where color-coded defects would induce MESs. In Figure 4a, each defect is assumed to be charge-neutral. We find that most of the individual defect-induced MESs cluster around the center of the bandgap and onwards. Additionally, the effective defect-defect interactions tend to broaden each MES feature, while adding a few more features near the band edges. We point out that the MESs closer to the band edges originate from the carbon dimer (C_BC_N) and nitrogen-substitutional oxygen (O_N). While the former has its lower-energy transition in the UV,[62] the latter does not have defect-defect transitions within the bandgap. As a result, these two defects are not directly probed in optical spectroscopy measurements, rendering their contributions to the experimental PL spectrum and time-correlations negligible. However, if present in sufficient quantities, EELS should still probe their MESs, which could explain the broad shoulder features near the band edges in Figure 1e.

While clusters of nearby defects in hBN should reach charge-neutrality in equilibrium, they are likely to be in their thermodynamic-favored charge states based on the local Fermi level. In hBN, this typically aligns closer to the conduction band[66] (between $E_g/2$ and E_g). Previous DFT calculations have characterized the thermodynamic charge-state stability for all defects considered herein.[59,67–72] Thus, we can use these results to recalculate the average DOS for the same "effective" defect cluster, but considering each individual defect in its thermodynamically most-stable charge state (Figure 4b). Clearly, enforcing these charge-state conditions results in a drastically different DOS for the same defect cluster configuration; here, most of the MESs cluster closer to the valence band edge. From the complex charge dynamics that occur during photo-excitation of single defects and defect clusters in other materials,[73–75] we can infer the defects in our model to be in a balance between the scenarios outlined in Figure 4a,b. Despite the difficulties in calculating precise alignment in the energies of defect-induced MESs from first-principles, we see a close resemblance between the overall shape of the averaged DOS from the defects considered, and the experimental results presented in Figure 1e (Supporting Information, Section S5). Overall, our first-principles modeling confirm that the defect constituents imaged through experiments are likely responsible for the observed MESs. Though a direct connection with the emission profile from such a defect cluster is not possible within our approximations, the positive correlation between the defect configuration and the observed MESs suggests a possible connection between these absorptive features and the observed PL emission from this site. Lastly, our results also suggest that possible (although weak) defect–defect interactions within these clusters could explain the slight differences between the experimental and calculated MES features, although further work along these lines is required for a decisive conclusion.

3. Conclusion

In summary, using a combination of optical and electron microscopy techniques, we have identified a set of absorptive defect-mediated electronic states within emissive hBN regions. Using high-resolution EELS in aberration-corrected STEM mode, we have captured the low-loss signal from the optically active site, which exhibits distinct features within the bandgap of hBN. Atomic resolution STEM-EELS of the same region reveals a defect structure consisting of boron vacancies and substitutional foreign species like carbon and oxygen, which are likely responsible for the defect-induced energy states observed in the low-loss signal. In addition, ab initio calculations also support the correlation between the imaged defect structure and defect-induced MESs in hBN. Our results shed light on the defect structure and absorptive features likely connected to the typical PL emission observed in hBN, opening possibilities for atomic-scale and optical control of hBN emitters for quantum technological applications.

4. Experimental Section

Sample Preparation: hBN flakes were exfoliated from bulk hBN crystal using scotch tape on Si substrate with 285 nm SiO_2 layer. Before the exfoliation, the substrate was cleaned in acetone and isopropyl alcohol. Different region of the hBN flake were irradiated with electron beam in an FESEM (FESEM, Jeol, JSM 7900F) using beam acceleration voltage of 5 kV and current 60 pA. The sample was subsequently annealed in an argon atmosphere at 850 °C for 2 h under continuous argon flow. The flow rate was adjusted to be at ∼ 20 sccm.

Optical Measurement: All our optical measurements were done at room temperature in a WITEC Alpha 300 confocal microscope customized with a HBT setup. A 532-nm continuous-wave (CW) laser was used for excitation, focused onto the sample using a 100× objective (NA∼ 0.95). A 532-nm cut-on dichroic was used to suppress the back-reflected laser from the light collected through the objective. The collected signal was fiber-coupled to a spectrometer (Princeton HRS 500) equipped with an Andor CCD camera. All spectra were acquired for 10 sec using a 600 lines/mm optical grating.

Low-Loss EELS Measurement: For STEM-EELS experiments, a spherical aberration-corrected Transmission Electron microscope (TEM) (JEOL, Neo ARM 200F) equipped with the cold field emission gun (c-FEG) was performed on the hBN sample. The accelerating voltage was kept at 80 kV, which is suitable to avoid sample contamination and also helpful to reduce the full width at half the maximum of the ZLP. Generally, the focused electron beam's convergence angle and probe current (at emission current 15.6 µA) should be 28 mrad and 18–20 pA. This parameter provides the FWHM ∼ 0.7 eV of ZLP. Further, to reduce the FWHM of ZLP, the emission current of the beam was reduced up approximately 4 µA. Using this modification in the experimental parameters, we could decrease the FWHM (up to 350 meV approximately) of ZLP. EELS spectra and spectral imaging were captured using the Gatan spectrometer (model 977) having a charge-coupled device (CCD) camera. The EELS aperture and energy dispersion were set to 2.5 mm and 50 meV/channel, respectively. The optimized pixel size and pixel dwell time for the spectral imaging were kept to 0.5 nm X 0.5 nm and 3 msec respectively.

STEM-EELS Measurements:: HAADF-STEM images and EELS spectra were acquired using a JEOL NEO ARM 200F (equipped with Cs corrector and a post-column Gatan EELS spectrometer). The system has a dedicated aberration-corrected STEM mode, combined with cold-field-emission guns operating at 80 kV. HAADF-STEM imaging was captured with the pixel size 0.0066 nm and dwell time 15 µs with the probe current (20pA). Also, HAADF inner and outer collection angles were set to 68 and 280 mrad, respectively. Using low-resolution STEM imaging, the location of the emitter was found by aligning the optical image of the flake (alignment is given in the Supporting Information, Section S1). At the same time, elemental EELS mapping was carried on the same location (see Figure 1). Second, EELS spectra and spectral images of sub-nanometer areas (1.192×0.894 nm^2, with 40×30 pixels) covering a few atoms were recorded with the Gatan EELS spectrometer. An EELS spectral mapping with zero-loss has been captured with dispersion of 0.24 eV/ch (perfectly covering boron, carbon, nitrogen and oxygen k edge signals), probe convergence angle of 28 mrad and collection angle of 12.5 mrad. Such dispersion really helps in aligning the boron and nitrogen k edge signals. Furthermore, to minimize the spatial drifting of the sample at the atomic resolution, we optimize the spectral image that has been acquired with a pixel size of 0.028 nm and a pixel time of 0.05 s.

First-Principles Calculations: All DFT calculations have been performed using the Vienna *ab-initio* simulation package (VASP) code.[76] In VASP, the projector-augmented wave (PAW) method is employed to treat core electrons in the form of atomic pseudo-potentials.[77] The remaining valence electrons are treated explicitly, in our case using the Heyd–Scuseria–Ernzerhof (HSE) functional to approximate exchange-correlation interactions, with the exact-exchange mixing parameter $\alpha = 0.31$.[78,79] We use the scheme of Grimme to treat van der Waals interactions, which are key in simulating bulk hBN within DFT.[80–82] The valence electrons are expanded in the plane-wave basis using a kinetic-energy cut-off of 500 eV. To ensure atomic positions and wave functions are sufficiently converged, the optimizations run until forces and energy changes are below 10^{-2} and 10^{-6}, respectively. Most of our computational parameters are based on previous work, which consistently provide reasonable treatment for the optoelectronic properties of carbon-related defects in hBN.[58,62,67,72] Each individual defect is embedded in a hexagonal $6 \times 6 \times 2$ hBN supercell, which is sufficiently large to have converged sampling of the Brillouin zone at the Γ-point only.

Supporting Information

Supporting Information is available from the Wiley Online Library or from the author.

Acknowledgements

S.S. and P.J. acknowledge an Institute Fellowship from the Indian Institute of Technology Jammu. B.C. acknowledges funding from SERB under the project grant SRG/2020/000563 and SAPTARISHI (Central Instrumentation Facility) at the Indian Institute of Technology Jammu. C.E.D. acknowledges support under NSF grant DMR-2237674. The Flatiron Institute is a division of the Simons Foundation.

Conflict of Interest

The authors declare no conflict of interest.

Author Contributions

S.S., P.J., and B.C. conceived the electron and microscopy measurements. S.S., P.J., and B.C. analyzed the experimental outcomes. K.W. and T.T. provided hBN crystals. G.I.L.M. and C.E.D. performed the *ab-initio* calculations and related analysis. All the authors discussed the results and contributed to the manuscript.

Data Availability Statement

The data that support the findings of this study are available in the supplementary material of this article.

Keywords

carbon, defects, hBN, mid-gap electronic states, STEM-EELS

Received: February 4, 2025
Revised: May 22, 2025

---

[1] I. Aharonovich, D. Englund, M. Toth, *Nat. Photonics* **2016**, *10*, 631.
[2] I. Aharonovich, E. Neu, *Adv. Opt. Mater.* **2014**, *2*, 911.
[3] A. Sipahigil, K. D. Jahnke, L. J. Rogers, T. Teraji, J. Isoya, A. S. Zibrov, F. Jelezko, M. D. Lukin, *Phys. Rev. Lett.* **2014**, *113*, 113602.
[4] J. L. Lyons, C. G. Van de Walle, *npj Comput. Mater.* **2017**, *3*, 12.
[5] J. Yuan, K. Wang, Y. Hou, F. Chen, Q. Li, *Photonics* **2023**, *10*, 544.
[6] B. Lienhard, T. Schröder, S. Mouradian, F. Dolde, T. T. Tran, I. Aharonovich, D. Englund, *Optica* **2016**, *3*, 768.
[7] D. Riedel, F. Fuchs, H. Kraus, S. Väth, A. Sperlich, V. Dyakonov, A. A. Soltamova, P. G. Baranov, V. A. Ilyin, G. V. Astakhov, *Phys. Rev. Lett.* **2012**, *109*, 226402.

[8] A. Lohrmann, N. Iwamoto, Z. Bodrog, S. Castelletto, T. Ohshima, T. J. Karle, A. Gali, S. Prawer, J. C. McCallum, B. C. Johnson, *Nat. Commun.* **2015**, *6*, 7783.
[9] N. T. Son, P. Carlsson, J. Ul Hassan, E. Janzén, T. Umeda, J. Isoya, A. Gali, M. Bockstedte, N. Morishita, T. Ohshima, H. Itoh, *Phys. Rev. Lett.* **2006**, *96*, 055501.
[10] N. R. Jungwirth, H. S. Chang, M. Jiang, G. D. Fuchs, *ACS nano* **2016**, *10*, 1210.
[11] T. T. Tran, K. Bray, M. J. Ford, M. Toth, I. Aharonovich, *Nat. Nanotechnol.* **2016**, *11*, 37.
[12] L. J. Martínez, T. Pelini, V. Waselowski, J. R. Maze, B. Gil, G. Cassabois, V. Jacques, *Phys. Rev. B* **2016**, *94*, 121405.
[13] T. Vogl, R. Lecamwasam, B. C. Buchler, Y. Lu, P. K. Lam, *Acs, Photonics* **2019**, *6*, 1955.
[14] N. V. Proscia, H. Jayakumar, X. Ge, G. Lopez-Morales, Z. Shotan, W. Zhou, C. A. Meriles, V. M. Menon, *Nano Photonics* **2020**, *9*, 2937.
[15] S. Sirohi, Ray D. Chawdhury, S. Narayanan, P. B. Bisht, *ACS Appl. Nano Mater.* **2024**, *8*, 254.
[16] M. Huang, J. Zhou, D. Chen, H. Lu, N. J. McLaughlin, S. Li, M. Alghamdi, D. Djugba, J. Shi, H. Wang, C. R. Du, *Nat. Commun.* **2022**, *13*, 5369.
[17] A. Gottscholl, M. Diez, V. Soltamov, C. Kasper, D. Krauße, A. Sperlich, M. Kianinia, C. Bradac, I. Aharonovich, V. Dyakonov, *Nat. Commun.* **2021**, *12*, 4480.
[18] Y. Chen, T. N. Tran, N. M. H. Duong, C. Li, M. Toth, C. Bradac, I. Aharonovich, A. Solntsev, T. T. Tran, *ACS Appl. Mater. Interfaces* **2020**, *12*, 25464.
[19] X. Gao, S. Vaidya, P. Ju, S. Dikshit, K. Shen, Y. P. Chen, T. Li, *ACS, Photonics* **2023**, *10*, 2894.
[20] T. Vogl, Y. Lu, P. K. Lam, *J. Phys. D: Appl. Phys.* **2017**, *50*, 295101.
[21] M. Grzeszczyk, K. Vaklinova, K. Watanabe, T. Taniguchi, K. S. Novoselov, M. Koperski, *Light Sci. Appl.* **2024**, *13*, 155.
[22] Z. Huang, R. G. Lee, E. Cuniberto, J. Song, J. Lee, A. Alharbi, K. Kisslinger, T. Taniguchi, K. Watanabe, Y. H. Kim, D. Shahrjerdi, *ACS nano* **2024**, *18*, 28700.
[23] X. Xu, Z. O. Martin, D. Sychev, A. S. Lagutchev, Y. P. Chen, T. Taniguchi, K. Watanabe, V. M. Shalaev, A. Boltasseva, *Nano Lett.* **2021**, *21*, 8182.
[24] S. Hou, M. D. Birowosuto, S. Umar, M. A. Anicet, R. Y. Tay, P. Coquet, B. K. Tay, H. Wang, E. H. T. Teo, *2D Mater.* **2017**, *5*, 015010.
[25] A. Gale, C. Li, Y. Chen, K. Watanabe, T. Taniguchi, I. Aharonovich, M. Toth, *ACS Photonics* **2022**, *9*, 2170.
[26] G. Grosso, H. Moon, B. Lienhard, S. Ali, D. K. Efetov, M. M. Furchi, P. Jarillo-Herrero, M. J. Ford, I. Aharonovich, D. Englund, *Nat. Commun.* **2017**, *8*, 705.
[27] N. V. Proscia, Z. Shotan, H. Jayakumar, P. Reddy, C. Cohen, M. Dollar, A. Alkauskas, M. Doherty, C. A. Meriles, V. M. Menon, *Optica* **2018**, *5*, 1128.
[28] N. Mendelson, D. Chugh, J. R. Reimers, T. S. Cheng, A. Gottscholl, H. Long, C. J. Mellor, A. Zettl, V. Dyakonov, P. H. Beton, S. V. Novikov, *Nat. Mater.* **2021**, *20*, 321.
[29] Y. Xiong, M. Mathew, S. M. Griffin, A. Sipahigil, G. Hautier, *Mater. Quantum Technol.* **2024**, *4*, 013001.
[30] M. Koperski, D. Vaclavkova, K. Watanabe, T. Taniguchi, Novoselov, K. S., M. Potemski, *Proc. Natl. Acad. Sci. USA* **2020**, *117*, 13214.
[31] R. Bourrellier, S. Meuret, A. Tararan, O. Stéphan, M. Kociak, L. H. Tizei, A. Zobelli, *Nano Lett.* **2016**, *16*, 4317.
[32] F. Hayee, L. Yu, J. L. Zhang, C. J. Ciccarino, M. Nguyen, A. F. Marshall, I. Aharonovich, J. Vučković, P. Narang, T. F. Heinz, J. A. Dionne, *Nat. Mater.* **2020**, *19*, 534.
[33] T. T. Tran, C. Elbadawi, D. Totonjian, C. J. Lobo, G. Grosso, H. Moon, D. R. Englund, M. J. Ford, I. Aharonovich, M. Toth, *ACS nano* **2016**, *10*, 7331.
[34] H. Henck, D. Pierucci, G. Fugallo, J. Avila, G. Cassabois, Y. J. Dappe, M. G. Silly, C. Chen, B. Gil, M. Gatti, F. Sottile, *Phys. Rev. B* **2017**, *95*, 085410.
[35] A. Y. A. T. O. Nagashima, N. Tejima, Y. Gamou, T. Kawai, C. Oshima, *Phys. Rev. B* **1995**, *51*, 4606.
[36] A. Nagashima, N. Tejima, Y. Gamou, T. Kawai, C. Oshima, *Phys. Rev. Lett.* **1995**, *75*, 3918.
[37] D. Usachov, V. K. Adamchuk, D. Haberer, A. Grüneis, H. Sachdev, A. B. Preobrajenski, C. Laubschat, D. V. Vyalikh, *Phys. Rev. B: Condens. Matter Mater. Phys.* **2010**, *82*, 075415.
[38] Y. Zhao, M. Tripathi, K. Čerņevičs, A. Avsar, H. G. Ji, J. F. G. Marin, C. Y. Cheon, Z. Wang, O. V. Yazyev, A. Kis, *Nat. Commun.* **2023**, *14*, 44.
[39] M. T. Greenaway, E. E. Vdovin, D. Ghazaryan, A. Misra, A. Mishchenko, Y. Cao, Z. Wang, J. R. Wallbank, M. Holwill, Y. N. Khanin, S. V. Morozov, *Commun. Phys.* **2018**, *1*, 94.
[40] Z. Qiu, K. Vaklinova, P. Huang, M. Grzeszczyk, K. Watanabe, T. Taniguchi, K. S. Novoselov, J. Lu, M. Koperski, *ACS nano* **2024**, *18*, 24035.
[41] D. Wong, J. Velasco Jr, L. Ju, J. Lee, S. Kahn, H. Z. Tsai, C. Germany, T. Taniguchi, K. Watanabe, A. Zettl, F. Wang, *Nat. Nanotechnol.* **2015**, *10*, 949.
[42] S. Yamashita, S. Fukushima, J. Kikkawa, R. Arai, Y. Kanitani, K. Kimoto, Y. Kudo, *APL Mater.* **2024**, *12*, 031101.
[43] T. Asano, M. Tezura, M. Saitoh, H. Tanaka, J. Kikkawa, K. Kimoto, *Appl. Phys. Express* **2022**, *15*, 076501.
[44] S. Wang, K. March, F. A. Ponce, P. Rez, *Phys. Rev. B* **2019**, *99*, 115312.
[45] S. X. Li, T. Ichihara, H. Park, G. He, D. Kozawa, Y. Wen, V. B. Koman, Y. Zeng, M. Kuehne, Z. Yuan, S. Faucher, *Commun. Mater.* **2023**, *4*, 19.
[46] O. L. Krivanek, M. F. Chisholm, V. Nicolosi, T. J. Pennycook, G. J. Corbin, N. Dellby, M. F. Murfitt, C. S. Own, Z. S. Szilagyi, M. P. Oxley, S. T. Pantelides, *Nature* **2010**, *464*, 571.
[47] J. H. Warner, Y. C. Lin, K. He, M. Koshino, K. Suenaga, *ACS nano* **2014**, *8*, 11806.
[48] K. Suenaga, H. Kobayashi, M. Koshino, *Phys. Rev. Lett.* **2012**, *108*, 075501.
[49] K. Suenaga, M. Koshino, *Nature* **2010**, *468*, 1088.
[50] S. Singla, P. Joshi, G. I. López-Morales, S. Sarkar, S. Sarkar, J. Flick, B. Chakraborty, *Nano Lett.* **2024**, *24*, 9212.
[51] A. Bhunia, P. Joshi, N. Singh, B. Chakraborty, R. V. Nair, *J. Phys. D: Appl. Phys.* **2024**, *57*, 395103.
[52] C. Ricolleau, J. Nelayah, T. Oikawa, Y. Kohno, N. Braidy, G. Wang, F. Hue, L. Florea, V. Pierron Bohnes, D. Alloyeau, *Microscopy* **2013**, *62*, 283.
[53] F. S. Hage, G. Radtke, D. M. Kepaptsoglou, M. Lazzeri, Q. M. Ramasse, *Science* **2020**, *367*, 1124.
[54] M. Xu, D. L. Bao, A. Li, M. Gao, D. Meng, A. Li, S. Du, G. Su, S. J. Pennycook, S. T. Pantelides, W. Zhou, *Nat. Mater.* **2023**, *22*, 612.
[55] M. Stöger-Pollach, H. Franco, P. Schattschneider, S. Lazar, B. Schaffer, W. W. Z. H. Grogger, H. W. Zandbergen, *Micron* **2006**, *37*, 396.
[56] A. M. Sánchez, M. Gass, A. J. Papworth, P. J. Goodhew, P. Ruterana, *Phys. Rev. B: Condens. Matter Mater. Phys.* **2004**, *70*, 035325.
[57] Y. Li, A. Chernikov, X. Zhang, A. Rigosi, H. M. Hill, A. M. Van Der Zande, D. A. Chenet, E. M. Shih, J. Hone, T. F. Heinz, *Phys. Rev. B* **2014**, *90*, 205422.
[58] M. E. Turiansky, A. Alkauskas, L. C. Bassett, C. G. Van de Walle, *Phys. Rev. Lett.* **2019**, *123*, 127401.
[59] S. Li, A. Gali, *J. Phys. Chem. Lett.* **2022**, *13*, 9544.
[60] D. I. Badrtdinov, C. Rodriguez-Fernandez, M. Grzeszczyk, Z. Qiu, K. Vaklinova, P. Huang, A. Hampel, K. Watanabe, T. Taniguchi, L. Jiong, M. Potemski, *Small* **2023**, *19*, 2300144.
[61] E. D. Mistry, D. Lubert-Perquel, I. Nevjestic, G. Mallia, P. Ferrer, K. Roy, G. Held, T. Tian, N. M. Harrison, S. Heutz, C. Petit, *Chem. Mater.* **2023**, *35*, 1858.

[62] M. Mackoit-Sinkevičienė, M. Maciaszek, C. G. Van de Walle, A. Alkauskas, *Appl. Phys. Lett.* **2019**, *115*, 212101.
[63] C. Jara, T. Rauch, S. Botti, M. A. Marques, A. Norambuena, R. Coto, J. E. Castellanos-Águila, J. R. Maze, F. Munoz, *J. Phys. Chem. A* **2021**, *125*, 1325.
[64] Z. Benedek, R. Babar, Á. Ganyecz, T. Szilvási, Ö. Legeza, G. Barcza, V. Ivády, *npj Comput. Mater.* **2023**, *9*, 187.
[65] M. Maciaszek, L. Razinkovas, *ACS Appl. Nano Mater.* **2024**, *7*, 18979.
[66] S. A. Marye, R. R. Kumar, A. Useinov, N. Tumilty, *Microelectron. Eng.* **2024**, *283*, 112106.
[67] M. Maciaszek, L. Razinkovas, A. Alkauskas, *Phys. Rev. Mater.* **2022**, *6*, 014005.
[68] S. A. Tawfik, S. Ali, M. Fronzi, M. Kianinia, T. T. Tran, C. Stampfl, I. Aharonovich, M. Toth, M. J. Ford, *Nanoscale* **2017**, *9*, 13575.
[69] C. E. Dreyer, A. Alkauskas, J. L. Lyons, A. Janotti, C. G. Van de Walle, *Annu. Rev. Mater. Res.* **2018**, *48*, 1.
[70] L. Weston, D. Wickramaratne, M. Mackoit, A. Alkauskas, C. G. Van de Walle, *Phys. Rev. B* **2018**, *97*, 214104.
[71] S. Li, A. Gali, *Front. Quantum Sci. Technol.* **2022**, *1*, 1007756.
[72] P. Auburger, A. Gali, *Phys. Rev. B* **2021**, *104*, 075410.
[73] G. Wolfowicz, C. P. Anderson, A. L. Yeats, S. J. Whiteley, J. Niklas, O. G. Poluektov, F. J. Heremans, D. D. Awschalom, *Nat. Commun.* **2017**, *8*, 1876.
[74] A. Lozovoi, H. Jayakumar, D. Daw, A. Lakra, C. A. Meriles, *Phys. Rev. Lett.* **2020**, *125*, 256602.
[75] Z. X. He, J. Y. Zhou, Q. Li, W. X. Lin, R. J. Liang, J. F. Wang, X. L. Wen, Z. H. Hao, W. Liu, S. Ren, H. Li, L. X. You, R. J. Zhang, Zhang, F. J. S. Tang, J. S. Xu, C. F. Li, G. C. Guo, *Nat. Commun.* **2024**, *15*, 10146.
[76] G. Kresse, J. Furthmüller, *Phys. Rev. B* **1996**, *54*, 11169.
[77] G. Kresse, D. Joubert, *Phys. Rev. B* **1999**, *59*, 1758.
[78] J. P. Perdew, K. Burke, M. Ernzerhof, *Phys. Rev. Lett.* **1996**, *77*, 3865.
[79] J. Heyd, G. E. Scuseria, M. Ernzerhof, *J. Chem. Phys.* **2003**, *118*, 8207.
[80] S. Grimme, J. Antony, S. Ehrlich, H. Krieg, *J. Chem. Phys.* **2010**, *132*, 154104.
[81] S. Grimme, S. Ehrlich, L. Goerigk, *J. Comput. Chem.* **2011**, *32*, 1456.
[82] D. G. Smith, L. A. Burns, K. Patkowski, C. D. Sherrill, *J. Phys. Chem. Lett.* **2016**, *7*, 2197.